High-resolution stress mapping of polycrystalline alumina compression using synchrotron X-ray diffraction

Seetha Raghavan[a]* and Peter Imbrie[b]

[a]University of Central Florida, Orlando, Florida, USA, and [b]Purdue University, West Lafayette, Indiana, USA. E-mail: sraghava@mail.ucf.edu

The ability to achieve uniform stress in uniaxial compression tests of polycrystalline alumina is of significance for the calibration of piezospectroscopic coefficients as well as strength studies in ceramics. In this study high-energy X-rays were used to capture powder diffraction profiles over a half-section of a polycrystalline alumina parallelepiped sample under an increasing uniaxial compressive load. The data were converted to strain and results were used for stress mapping of the sample. Stress maps from the study quantify the higher stresses at the sample–platen contact interface and reveal the evolution of the stress distribution in these specimens with load. For the geometry of the samples used, at the center section of the specimen the overall magnitudes of the compressive stresses were found to be 20% higher compared with the average expected theoretical stress based on the applied load and cross-sectional area. The observed compressive stresses at the corners of the parallelepiped specimen were 62% higher and shear stresses were observed at the specimen interface to the load mechanism. The effects, seen at the interface, can lead to premature failure at these locations and can affect the accuracy of calibration of spectral peaks with stress as well as compression strength measurements. The results provide important information that can be used to establish guidelines on material and geometry considerations in developing compression tests on high-strength ceramics.

Keywords: X-ray diffraction; stress mapping; alumina.

1. Introduction

Compression testing for high-strength ceramics such as polycrystalline alumina involves large applied loads on small cross-sectional specimens. The effectiveness of these tests in achieving uniform compression can be assessed from variations in the recorded compression strength of alumina (94% purity), which ranges from −1.89 to −3.43 GPa (Lankford, 1977; ASTM, 1983; Tracy, 1987). The challenge in such studies is that compression strengths are over an order higher than tensile strengths in these materials leading to premature failure if perfectly uniform compression is not achieved. Factors of significance are the alignment of the applied load, stress concentration factors at the specimen interfaces and compliance effects caused by the elastic mismatch between the specimen and load mechanism (Tracy, 1987; Dunlay *et al.*, 1989). The aspect ratio and end constraints in compression testing of brittle materials have an influence on the deformation and fracture mechanisms (Zeuch, 1992; Castaing *et al.*, 1998).

The motivation of the stress mapping described in this study is the development of photo-stimulated luminescence spectroscopy as a stress measurement method (Raghavan & Imbrie, 2009). The *R* lines that form part of the spectral signature of alumina have been utilized for their stress dependency, from early applications in monitoring stresses in diamond-anvil cells (Forman *et al.*, 1972) to their later widespread use in measuring stresses in the thermally grown oxide (TGO) of thermal barrier coatings (TBCs). These coatings provide protection against high-temperature environments (Gell *et al.*, 2004; Nychka & Clarke, 2001). The measurement of stresses in TGO is significant for the life prediction of TBCs in components such as gas turbine engine blades (Clarke *et al.*, 1997). Recent findings on the piezospectroscopic nature of the vibronic bands within the spectra of alumina (Raghavan & Imbrie, 2009; Abbasova *et al.*, 2005) indicate the potential of this method for the measurement of the complete stress state in the material. Here, achieving successful compression tests in alumina is critical in order to correctly establish the piezospectroscopic coefficients, which describe how the spectral

peaks shift with applied stress on the material. Since the introduction of the method, piezospectroscopic effects have been studied by loading specimens in uniaxial compression (Schawlow, 1961; Kaplyanskii & Przhevuskii, 1962; Feher & Sturge, 1968; He & Clarke, 1995). In these tests, the spectral peakshifts were calibrated against the theoretical applied stress, using the measured load and the cross-sectional area and assuming uniform compression. However, little has been reported on measures to ensure uniform compression in the test specimen. Furthermore, the maximum loads applied are generally well below the reported compressive strength of the material, providing little opportunity to use the failure locations to establish whether the sample is experiencing non-uniform stresses. He & Clarke (1995) addressed this unknown by comparing spectral measurements at the four corners in the plane of the test section to assess uniformity. In *ex situ* experiments using high-energy X-ray diffraction (XRD) and photo-stimulated luminescence spectroscopy (PSLS; Raghavan & Imbrie, 2009), the spectral peaks were calibrated with the stress established from XRD strain measurements, illustrating the complementary nature of the two methods. With synchrotron X-ray diffraction, improved spatial resolution with extremely short collection times have improved the quality of strain measurement data attainable today (Korsunsky *et al.*, 1998). Using a two-dimensional detector to measure the interplanar spacing of the lattice, which acts as an internal strain gage (Noyan & Cohen, 1987), high-resolution strain data, of the order 10^{-4}, can be achieved. The estimated strain measurement variation is less than 10^{-4} as indicated by previous studies at the synchrotron (Jakobsen, 2006; Haeffner, 2005). Using the X-ray elastic constants, stress maps can then be established over the sample under applied load.

While piezospectroscopic measurements are the subject of significance in this work, the results are of significance to compression strength measurements in high-strength ceramics and composites in general. Studies conducted by Tracy to evaluate a new compression test method for high-strength ceramics compared strength results obtained using three types of specimens: the ASTM standard specimen (ASTM, 1983), a three-piece specimen system by Lankford (1977), and his one-piece specimen. While Lankford's three-piece specimen system was made up of a section similar to the ASTM specimen and included contact end caps of the same material, the one-piece specimen integrated the design into a complete dumbell-shaped specimen. His tests revealed that the failure mode of the other specimens was hugely affected by the interface between the gage section and the contact cylinders, thus resulting in lower compressive strength values than the one-piece dumbell specimen. The average compressive strength value of polycrystalline alumina was −2.38 GPa with the ASTM standard test specimen, while the one-piece specimen gave a compressive strength of −3.43 GPa. In addition, some of the lower-strength test fractures were observed to initiate at the gage/contact cylinder interface and strain gage results showed a non-uniform state of stress. In the case of the three-piece system it was concluded that the alignment for a multiple-piece specimen was critical to the

ability to obtain a uniform state of stress. The micrometer-sized intense beams of high spatial resolution provided by synchrotron X-rays are ideal for mapping stresses in such compression tests. The stress mapping presented in this work sheds light on the distribution and uniformity of the stress within the ceramic sample including the contact surfaces of the load application.

2. Theory

The general methods of stress determination using synchrotron XRD for strain studies have been previously described (Hauk, 1997; Wanner & Dunand, 2000; Raghavan & Imbrie, 2008, 2009) and are summarized here. As the X-rays impinge the sample, the interplanar spacing of the diffraction planes are determined using Bragg's law. The distortion of the rings of diffraction patterns, with compression, provides information on the strain given by the ratio of the change in d-spacings and the original d-spacing of an unstrained lattice. The diameter of the ring is related to the lattice spacing using simple trigonometry of the diffraction set-up [equation (2)], and with Bragg's law gives

$$\theta = \frac{1}{2}\arctan\left(\frac{D}{2L}\right), \tag{1}$$

where θ is the angle between the incident ray and the scattering planes, D is the diameter of the diffraction ring and L is the sample to detector distance,

$$d = \frac{\lambda}{2\sin[(1/2)\arctan(D/2L)]}. \tag{2}$$

Equation (2) can be simplified for small Bragg angles (high-energy X-rays) as

$$d \simeq \frac{\lambda L}{D}. \tag{3}$$

Hence, the strain for a lattice plane (the reference or unstressed state denoted with subscript 0) is expressed in terms of the diffraction ring diameter as equation (4) (Korsunsky *et al.*, 1998; Wanner & Dunand, 2000). This is the widely used equation in strain determination using X-ray diffraction with a two-dimensional area detector,

$$\varepsilon = \frac{d - d_0}{d_0} \simeq \frac{D_0 - D}{D_0}. \tag{4}$$

The experimental set-up and orthogonal coordinate systems used to derive equations for strain determination are shown in Fig. 1. The axes S_i define the surface of the sample with S_1 and S_2 on the surface. The axes L_i define the laboratory system with L_3 in the direction of the normal to the planes (hkl), whose interplanar spacing d will be measured. L_2 makes an angle φ with S_2 and is in the plane which is defined by S_1 and S_2. When the interplanar lattice spacing d is obtained from the diffraction peak for a given reflection crystallographic plane, the strain component along L_3 can be obtained using the formula (Hauk, 1997)

$$(\varepsilon'_{33})_{\varphi\psi} = \frac{d_{\varphi\psi} - d_0}{d_0}, \tag{5}$$

where d_0 is the unstressed lattice spacing (primed quantities refer to the laboratory system while unprimed quantities refer to the sample coordinate system).

The strains may be expressed in terms of the strains ε_{ij} in the sample coordinate system through a tensor transformation as follows,

$$(\varepsilon'_{33})_{\phi\psi} = a_{3k}a_{3l}\varepsilon_{kl}, \tag{6}$$

where a_{3k}, a_{3l} are the direction cosines between L_3, S_k and L_3, S_l.

The direction cosine matrix is

$$a_{jk} = \begin{pmatrix} \cos\varphi\cos\psi & \sin\varphi\cos\psi & -\sin\psi \\ -\sin\varphi & \cos\varphi & 0 \\ \cos\varphi\sin\psi & \sin\varphi\sin\psi & \cos\psi \end{pmatrix}. \tag{7}$$

Substituting for a_{3k}, a_{3l} in (6) gives the fundamental equation of X-ray strain determination,

$$\begin{aligned} (\varepsilon'_{33})_{\varphi\psi} = \frac{d_{\varphi\psi} - d_0}{d_0} &= \varepsilon_{11}\cos^2\varphi\sin^2\psi + \varepsilon_{12}\sin 2\varphi\sin^2\psi \\ &\quad + \varepsilon_{22}\sin^2\varphi\sin^2\psi + \varepsilon_{33}\cos^2\psi \\ &\quad + \varepsilon_{13}\cos\varphi\sin 2\psi + \varepsilon_{23}\sin\varphi\sin 2\psi. \end{aligned} \tag{8}$$

Three basic $d_{\varphi\psi}$ *versus* $\sin^2\psi$ behaviors are observed in polycrystalline materials. Linear behavior is predicted when $\varepsilon_{13}, \varepsilon_{23}$ are zero, while data exhibiting oscillatory behavior cannot be predicted by (8) without modification. When either or both $\varepsilon_{13}, \varepsilon_{23}$ are non-zero, d measured at positive and negative ψ will be different due to the argument $\sin 2\psi$ associated with the terms causing ψ splitting.

In this case, to obtain the six strain components the following solution given by Dolle and Hauk (Dolle & Hauk, 1977; Hauk, 1997) may be used. Defining the parameters a_1 and a_2,

$$\begin{aligned} a_1 &= \frac{1}{2}\left(\varepsilon_{\varphi\psi+} + \varepsilon_{\varphi\psi-}\right) = \left(\frac{d_{\varphi\psi+} + d_{\varphi\psi-}}{2d_0} - 1\right) \\ &= \left(\varepsilon_{11}\cos^2\varphi + \varepsilon_{12}\sin 2\varphi + \varepsilon_{22}\sin^2\varphi - \varepsilon_{33}\right)\cdot\sin^2\psi + \varepsilon_{33}, \end{aligned} \tag{9}$$

$$\begin{aligned} a_2 &= \frac{1}{2}\left(\varepsilon_{\varphi\psi+} - \varepsilon_{\varphi\psi-}\right) = \left(\frac{d_{\varphi\psi+} - d_{\varphi\psi-}}{2d_0}\right) \\ &= \left(\varepsilon_{13}\cos\varphi + \varepsilon_{23}\sin\varphi\right)\sin|2\psi|, \end{aligned} \tag{10}$$

where $\psi_- = (-1)\cdot\psi_+$ and $\sin 2\psi_+ - \sin 2\psi_- = 2\sin|2\psi|$.

Equation (9) predicts a linear variation of a_1 with $\sin^2\psi$ while (10) shows a linear variation of a_2 with $\sin|2\psi|$. Hence, if $d_{\varphi\psi}$ data are obtained over a range of $\pm\psi$ at three φ rotation angles (0, 45 and 90°), and a_1 *versus* $\sin^2\psi$ and a_2 *versus* $\sin|2\psi|$ are plotted for all ψ, the six strain quantities can be obtained from the slopes and intercepts.

3. Experiment

The experiments for this study were conducted at the 5-BM-D beamline operated by the Dupont-Northwestern collaborative access team (DND-CAT) at the Advanced Photon Source, Argonne National Laboratory. This is a bending-magnet beamline. The experimental set-up for high-energy transmission experiments has been described in detail in the literature (Wanner & Dunand, 2000; Raghavan & Imbrie, 2009) and is shown here in Fig. 1.

The specimen was irradiated with a monochromatic parallel beam of high-energy X-rays and complete diffraction rings recorded by a two-dimensional detector. The beam energy was set to 68 keV photons which corresponds to a wavelength of $\lambda = 0.18233$ Å. The beam dimensions were set to 0.3×0.3 mm using slits. The diffraction pattern produced from the illuminated volume was detected using an on-line image-plate detector (MAR345, Marresearch GmBH, Norderstredt, Germany) at approximately 1370 mm from the sample. The detector is a circle of 345 mm diameter corresponding to a pixel size of 150×150 µm and an area of 0.093 m^2. The detector-to-sample distance was chosen based on the fact that large distances reduce systematic strain errors due to any sample displacement and increase strain resolution. The two-dimensional detector enabled the acquisition of vast amounts of data in fast readout times.

The specimen used for the X-ray experiments was commercially available polycrystalline alumina (Coorstek AD-995) with an average reported grain size of 6 µm. This was machined to rectangular parallelepiped-shaped samples with dimensions $1.8 \times 2 \times 4$ mm for loading. The
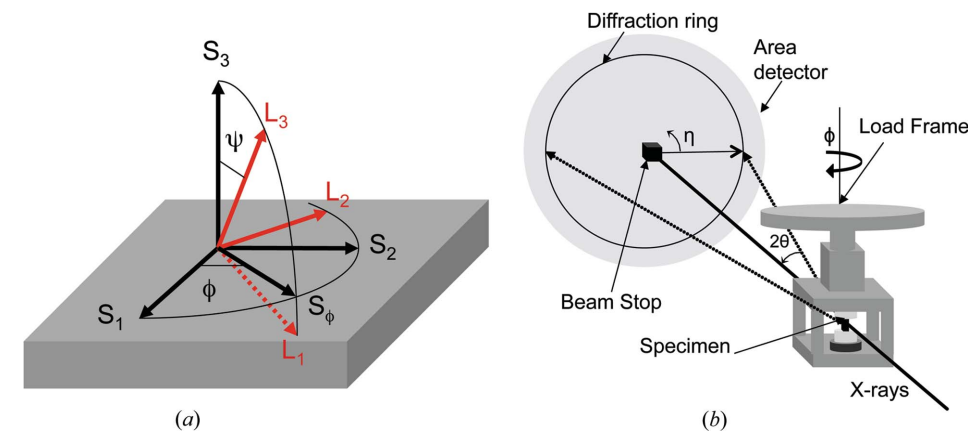

Figure 1
(a) The laboratory coordinate system L_i based on the *hkl* plane is related to the specimen coordinate system S_i through the angles ψ and φ; (b) the XRD experimental set-up in transmission mode showing the azimuth and diffraction angles.

specimen aspect ratio was chosen based on standards for ceramics (ASTM, 2006). Parallelism of the top and bottom load-bearing surfaces was better than 0.05° and the perpendicularity of the sides of the specimen with respect to the load-bearing surfaces was better than 0.06°. The load frame used for the compression tests had a large spindle head leadscrew of 80 threads per inch, for accurate load application with small vertical movement. A load transfer ball between the lead screw and the load piston inside the chamber of the upper plate helped to ensure the perpendicularity of the loading while minimizing any effects of rotational motion on the system. The specimen was placed at the center of the load path using an alignment fixture with two sapphire platens to prevent any damage on the contact surfaces of the load piston. A button-type compression load cell (EL Load Cell, Model ELA-B2E-2KL, Entran Devices, Fairfield, NJ, USA) with a range of 10000 N and 0.25% accuracy at full capacity was used with an automatic digital reader (Model MM50-L Entran Devices) to read the applied load on the specimen. The entire load frame was attached onto a translational stage to allow for precise movement of the load frame, which is essential for positioning the X-rays onto the desired location on the specimen for mapping.

The stress mapping of the polycrystalline specimen was carried out by defining a grid of points over the upper half of the specimen surface assuming symmetrical conditions for the lower half. The layout of the stress-mapping locations are shown in Fig. 2. Seven horizontal measurements were made across the specimen by stepping the sample in the x direction and taking a diffraction pattern at each (0.3 mm) step. These measurements were repeated over eight rows vertically upward towards the top edge of the specimen in contact with

Figure 2
The grid layout for strain mapping of the polycrystalline alumina specimen. X-ray readings are taken over (a) 56 locations at $\varphi = 90°$ before the specimen is rotated to take (b) 40 readings at $\varphi = 0°$. The region of interest is the $\varphi = 90°$ rotation angle for which the (c) stress maps will be plotted as shown in the example.

the sapphire platen by stepping the sample y direction (0.3 mm) for each row. Any shear effects in the specimen at the contact surface with the platen was to be captured by these measurements. Hence, in total 56 locations were studied in one direction ($\varphi = 90°$) before rotating the specimen 90° and taking the measurements again ($\varphi = 0°$). In this rotated direction, 40 locations were measured due to the reduced thickness (1.8 mm) with five locations in the horizontal direction in 0.4 mm steps and eight rows in the y direction (0.3 mm). Only two rotations were performed due to the constraints of the load frame supports in the path of the beam at other angles. The diffracting volume over which the average measurement was made was ~0.162 mm³ for the $\varphi = 90°$ face. This ensures a sufficient number of grains (individual grain size of approximately 6 µm) were probed.

4. XRD analysis and results

The methodology for the analysis of XRD data has already been described in detail in the existing literature (Almer et al., 2003; Raghavan & Imbrie, 2008, 2009) and is summarized here. The theory described for XRD stress determination assumes that the wavelength of the X-ray and the sample-to-detector distance remains unchanged over the course of the experiment. While the synchrotron X-ray source is relatively stable making the first assumption reasonable, the sample-to-detector distance can change due to motion during loading or Poisson's effect on the loaded specimen. However, earlier studies (Ott et al., 2005; Wanner & Dunand, 2000), using a calibration material in conjunction with the loaded specimen, showed that the effects of the loading on the sample-to-detector distance was small and similar results were obtained with and without correction for the distance. The negligible effect of small changes in sample-to-detector distance is especially evident with the small order of strains that are seen for alumina. The program Fit2d (Hammersley, 1998) was used to establish the sample-to-detector distance with zero-load case data using the calibration tool since alumina is a known calibrant material. This also established the detector tilt with respect to the beam. The beam center was determined for the representative center location for each load using the tilt function in Fit2d. Although it is expected that there is residual stress within the sample in the unloaded state due to the manufacturing process, the aim in this study was to measure the change in stress over the sample due to the applied loading and compare this with the similar change measured through piezospectroscopy.

The outermost ring corresponding to the (116) planes of alumina was used for the analysis since diffraction lines at greater Bragg angles are generally more sensitive to strain. The distinct ring-like diffraction patterns shown in Fig. 3 were transformed into linear plots of azimuthal angle against radial distance (radial plots) using the integrate function in Fit2d. The effects of strain on the outermost ring appear as 'wiggling' lines in the radial plots. This is because, as the load increases, the specimen is compressed and the d-spacing along the load axis (90 and 270° azimuth angles) decreases. This results in an
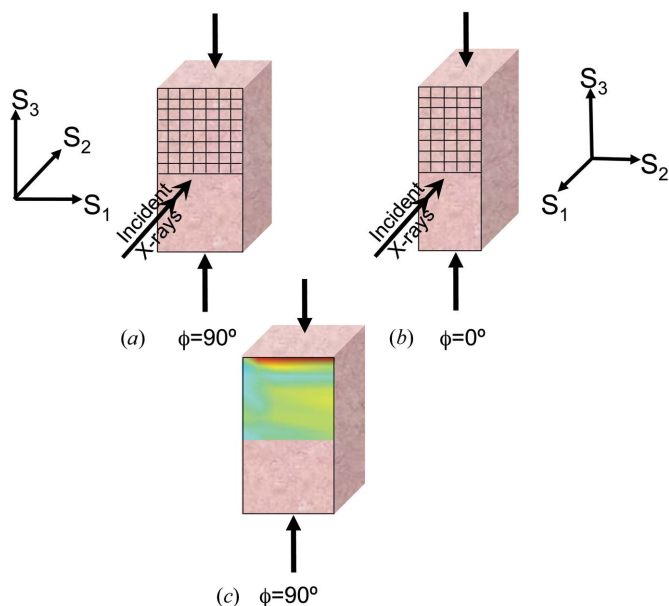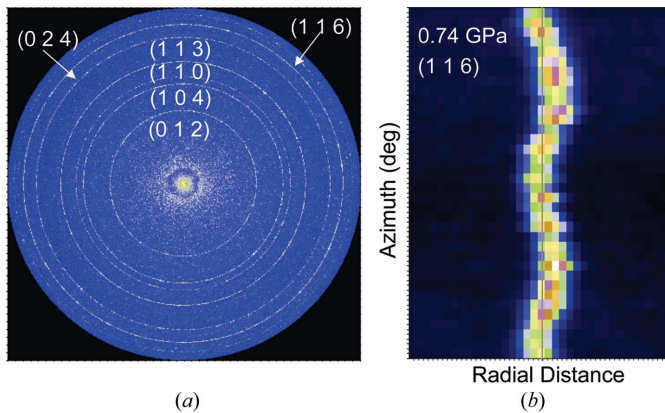
Figure 3
(a) The diffraction rings identified according to *hkl*. The (116) ring was chosen for the strain computations as the outer rings are more sensitive to strain; (b) the (116) ring converted to a radial plot illustrating the presence of strain.
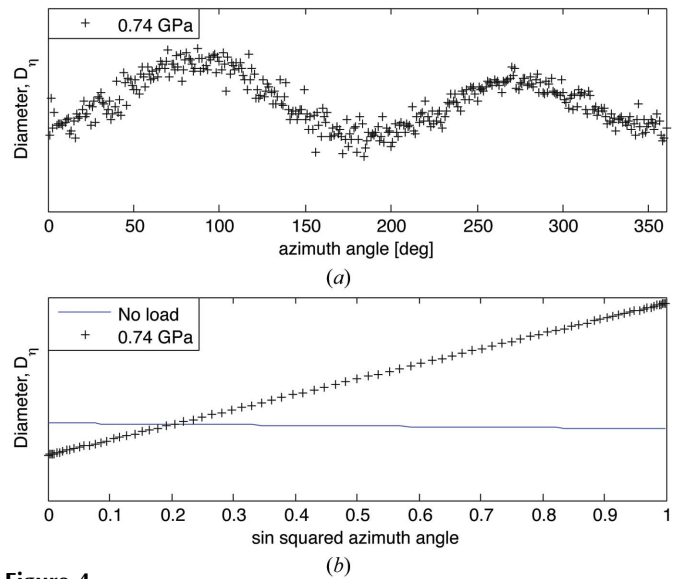

Figure 4
The diffraction ring diameter *D*, plotted against (a) the azimuth angle and (b) the sine-squared azimuth angle illustrated for the center point on the specimen under an applied stress of 0.74 GPa.

increase in the Bragg angle at these locations and hence the radial distances at these locations are greater. The centroids of the diffraction patterns in these radial plots were then found by a least-squares routine for each azimuthal position (Almer *et al.*, 2003). This routine (provided by sector 1, Argonne National Laboratory) fits a pseudo-Voigt function to the chosen peak (ring) at each azimuth angle. In this case the fitting was carried out at intervals of 1° around the azimuth of the diffraction pattern achieving minimum tolerances with directional derivatives less than 1×10^{-6}. The addition of the resulting centroid peak positions of diametrically opposite peaks gives the ring diameter at each azimuth angle and is presented in Fig. 4. The use of the diameter rather than the radius for strain evaluation ensures the results are not particularly sensitive to the choice of beam center (Korsunsky *et al.*, 1998). The uncertainty in the peak position is conservatively estimated to be at most $\pm 1/2$ pixel (Jakobsen, 2006; Jakobsen *et al.*, 2007), and relates to the uncertainty in strain for the (116) ring through equation (3) as $\pm 2.4 \times 10^{-4}$ and correspondingly in stress as ± 93 MPa.

The strain components ε_{33}, ε_{22} and ε_{23} were obtained for all 56 locations on the grid for $\varphi = 90°$ shown in Fig. 2 using the relation in equation (1) and plotting a_1 *versus* $\sin^2 \psi$ and a_2 *versus* $\sin |2\psi|$ described in equations (9) and (10). The strain values ε_{11} and ε_{13} from $\varphi = 0°$ were averaged horizontally across the grid to represent a value for each row on the $\varphi = 90°$ rotation. The in-plane shear strain ε_{12} is

assumed to be zero. The strain information was then used to obtain the stress values using the generalized Hooke's Law and X-ray elastic constants (Hauk, 1997) for the material and plotted as stress maps for each corresponding applied compressive stress. The stress maps for the components of stress evaluated are shown in Figs. 5–8.
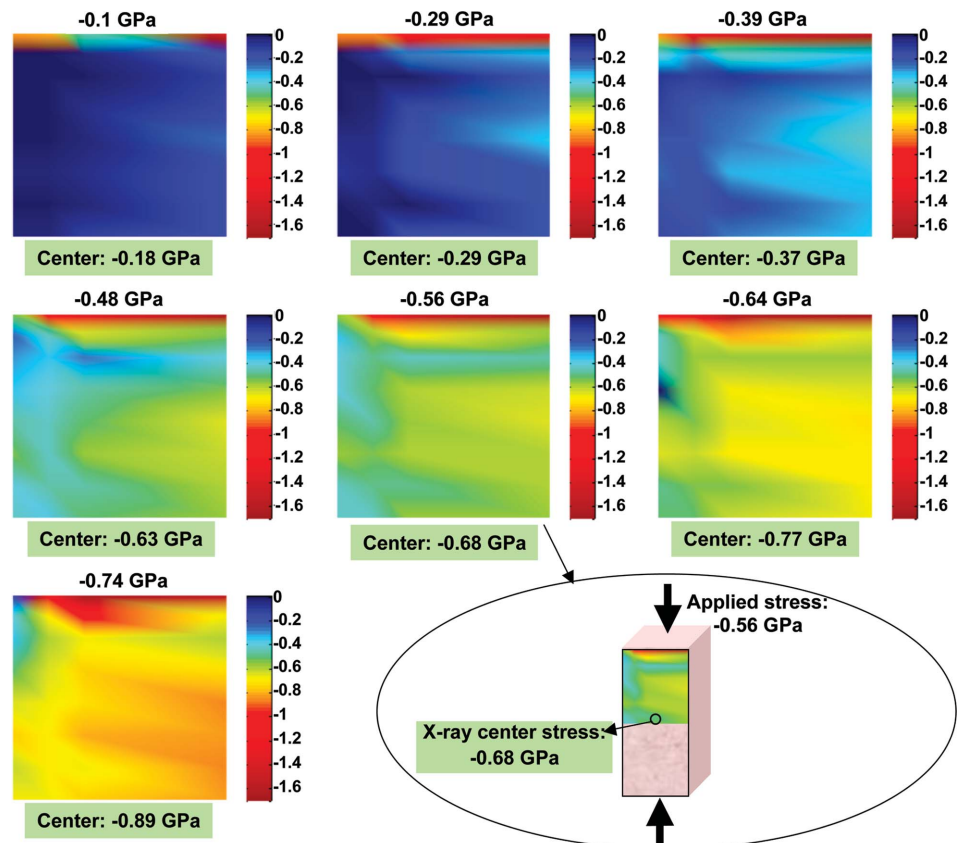

Figure 5
σ_{33} stress map of a half-specimen ($\varphi = 90°$) at increasing applied compressive stress in the S_3 direction.
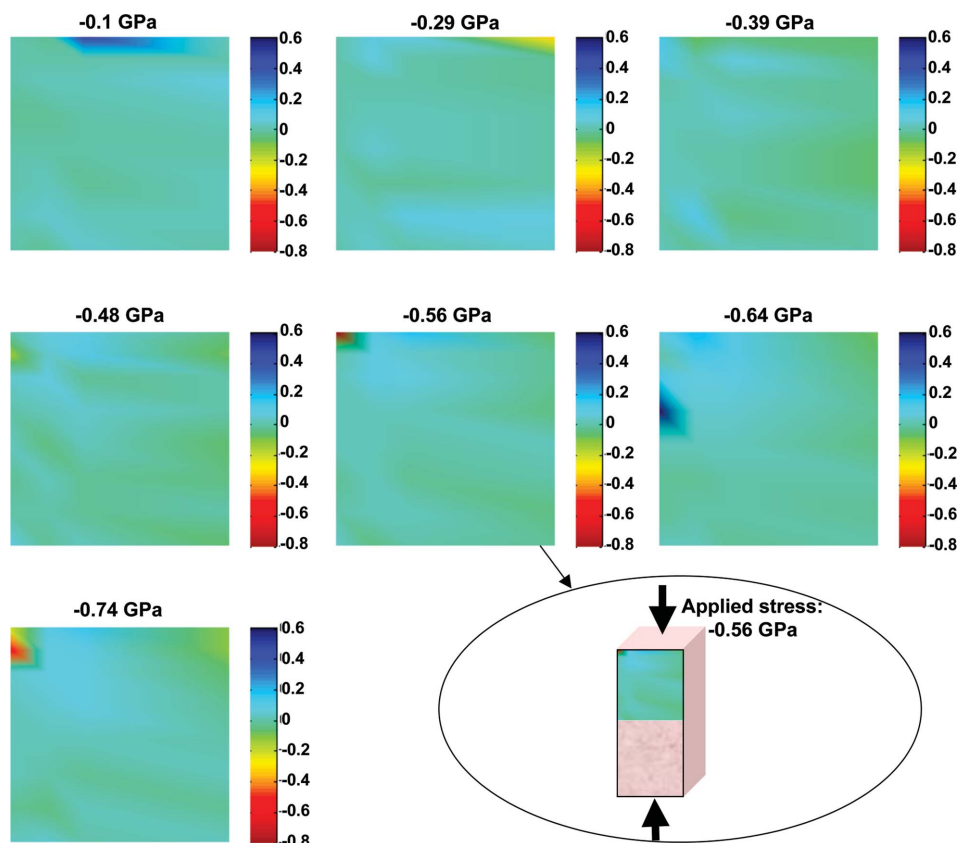
Figure 6
σ_{23} stress map of a half-specimen ($\varphi = 90°$) at increasing applied compressive stress in the S_3 direction.

At the $\varphi = 90°$ rotation the stress components σ_{33}, σ_{22} and σ_{23} were obtained, and at the $\varphi = 0°$ rotation the remaining stress components σ_{11} and σ_{13} were obtained. Fig. 5 shows the σ_{33} mapping of the 56 locations over the half-specimen and its evolution with the theoretical applied stress (applied load/cross-sectional area) indicated above each map. The applied stress range was from 0 to 0.74 GPa. The XRD measured stress value of the grid point at the center of the specimen is indicated below the specimen. Here, the compressive stresses within the specimen in the loading direction σ_{33} show higher values of stress compared with the applied stress in most regions and this is especially significant at the contact surface where the load is applied. At this surface, higher compressive stresses with a maximum of 1.2 GPa for an applied stress of 0.74 GPa were observed. A higher σ_{33} value was observed on the right upper corner of the specimen at initial loads which eventually reduced to a low value at higher loads. The corresponding shear stress σ_{23} (Fig. 6), relatively small in the range of 0.005 GPa and less throughout the specimen, increased at this corner to a high value of approximately 0.6 GPa at the higher loads. Consequently, a slight asymmetry in stresses was observed throughout the specimen with the right side of the specimen experiencing lower σ_{33} (Fig. 5) values.

The σ_{11} and σ_{22} stresses in the material represent the expansion due to Poisson's effect in the lateral direction. Low tensile stresses are expected and observed in the results, with

alumina having a Poisson's ratio of 0.23 (Dunlay *et al.*, 1989). The maximum tensile stresses in the center region were in the range 0.1–0.2 GPa for σ_{11} and σ_{22}. However, the end effects on the specimen–platen surface was seen in these lateral stresses to have maximum compressive values close to 0.2 GPa for σ_{11} and as high as 1 GPa for σ_{22}. The stress maps show the similar trend of slight asymmetry in both σ_{11} and σ_{22} (Figs. 7 and 8) while shear stress σ_{13} was generally found to be negligible throughout the specimen. Besides the anomaly at the contact surface and edge, the remaining shear stresses are close to zero at the center of the specimen or test section.

Besides providing complete stress components for several locations in the specimen, with the assumption that $\sigma_{12} = 0$, the data presented here provide valuable information on the possible stress distribution issues that can be faced in uniaxial compression tests of this nature where a small high-strength ceramic specimen is loaded at a high uniaxial compression load. The maps provide a visual understanding of the stresses at the contact surface with the platen and their evolution with load. The effects at the contact surface can be due to a number of factors such as the specimen surface irreguliarities, non-parallelism of the loading surfaces and non-uniform load transfer between the load frame and the test specimen. These are discussed in detail in §5.

5. Discussion

The stress maps from the high-energy XRD studies of polycrystalline alumina in compression indicate non-uniform stresses as well as high and anomalous stresses at the specimen–platen interface. The contributing factors are presented and elaborated here. In studies leading to the development of a compression test method for high-strength ceramics (Tracy, 1987; Dunlay *et al.*, 1989), issues such as stress concentration factors at the specimen interfaces, specimen alignment and parallelism of load surfaces were highlighted to have significant effects on the compression tests of high-strength ceramics. The importance of specimen length to width ratio and end constraints in the compression testing of brittle materials has been further highlighted by Zeuch (1992). End effects or the effects of highly constraining end conditions can lead to changes in deformation and fracture mechanisms. The friction at the interface can lead to shape changes in
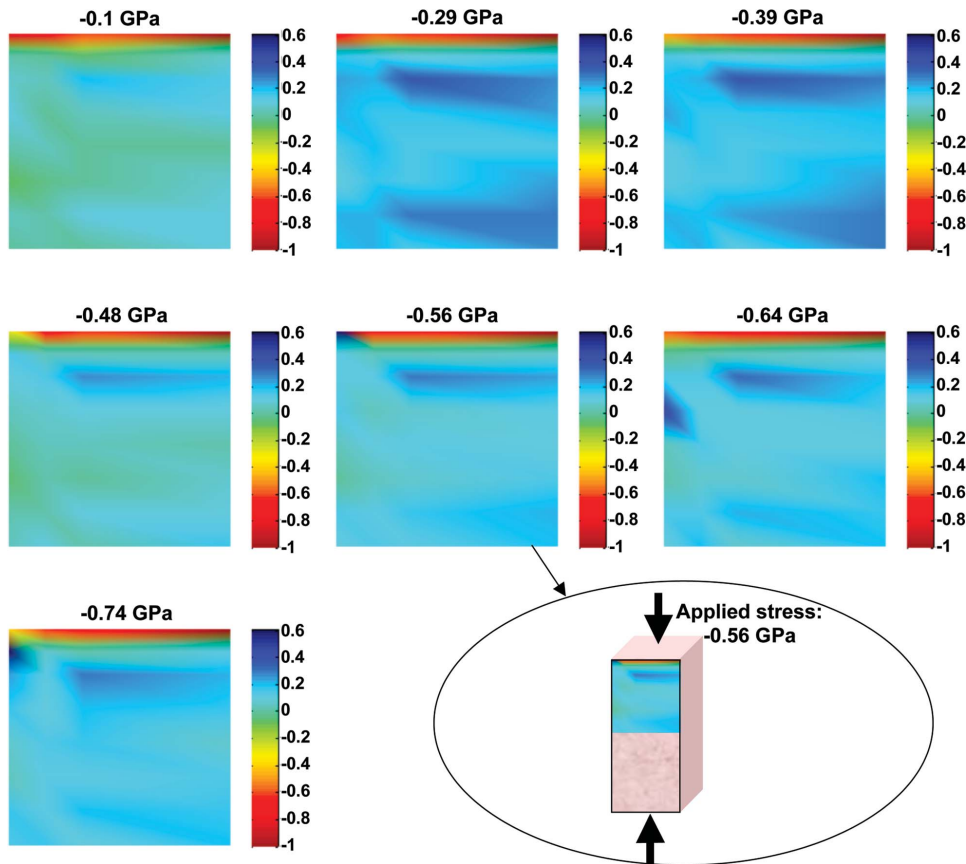
Figure 7
σ_{22} stress map of a half-specimen ($\varphi = 90°$) at increasing applied compressive stress in the S_3 direction.

Besides the effects of non-parallelism, local stresses due to irregularities in the mating surfaces of the specimen and platen can lead to concentrated high stresses. Surface polishing and requirements for exceedingly close tolerances are solutions to alleviate these problems. The sample used in this study is of a parallelepiped geometry having corners that are susceptible to errors in tolerance. A cylindrical specimen is the preferred geometry to reduce these errors.

The interface friction effects, if significant, can cause localized stresses affecting the distribution of stresses within the specimen. Based on the friction studies of single-crystal and polycrystalline material by Buckley (1966), single-crystal friction coefficients (sapphire on sapphire) were lower for the basal plane orientation (*c* axis) compared with the *a* and *m* axis. The polycrystalline friction coefficient (polycrystalline alumina on itself) was found to be intermediate between the two values. While the surfaces of the specimen were lubricated in an effort to reduce friction effects, the effect of the high loads on the friction at the contact surface is unknown. With the appropriate specimen aspect ratio, it is expected that friction effects at the interface should not affect the uniformity at the test section.

compression which may induce the start of failure through slip (Castaing *et al.*, 1998). The test specimen geometry adopted in our studies was motivated by the parallelepiped specimen geometry used for calibration of piezospectroscopic coefficients. The aspect ratio was based on ASTM standard test methods for compressive strength of ceramics and methods for high modulus materials (ASTM, 2002, 2006). While the quantitative results may be specific to the details of the specimen geometry, general effects and solutions to alleviate the problems can be derived from this study.

5.1. Specimen end effects

The effect of non-parallelism of the loading surfaces, either of the specimen or the platen in contact with the specimen, will result in eccentric loading and therefore bending of the specimen. This results in asymmetric stresses and stress concentrations that can lead to premature failure. Dunlay's error analysis for failure due to non-parallelism resulted in a requirement of the surface slope to be within 0.001 rad for bending effects to be negligible (Dunlay *et al.*, 1989). While the parallelism tolerance of the machined sample meets this requirement, the multiple surfaces are in contact in this experiment; including the load frame to platen and platen to sample interfaces requires a more stringent assessment of parallelism requirements.

5.2. Specimen aspect ratio

The test specimens used in our experiments were of an aspect ratio of 2.0 and the loading was performed using sapphire platens which were the contact cylinders between the load frame and the specimen. The contact cylinders were used to aid in the distribution of load to reduce detrimental end effects (ASTM, 2006). Although the probability of failure in other modes such as buckling is reduced by a shorter gage length, the complicated state of stress that exists at the extremities of the specimen due to the clamping forces that prevent lateral expansion can extend throughout the specimen because of a small aspect ratio (Reiss *et al.*, 1983). This effect was first studied by Pagano & Halpin (1968) in tensile tests of anisotropic bodies where it was concluded that the aspect ratio of the specimen and gripping mechanism were the principal reasons for the non-existence of a uniform stress state. The studies indicate here the need for an aspect ratio larger than 2.0 for an effectively uniform stress in the test section. A systematic study varying the aspect ratio and observing its

effects on the stress distribution can provide an upper bound to ensure buckling is avoided.

5.3. Significance of findings on piezospectroscopic studies of polycrystalline alumina

Over the last four decades various researchers have established *R*-line peakshifts against theoretical stress, presented here in Table 1. In order to accurately calibrate the spectral shifts of the *R*-lines from polycrystalline alumina, the peak positions were plotted against stress from the synchrotron XRD strains measured, as reported in our previous work (Raghavan *et al.*, 2008; Raghavan & Imbrie, 2009) and highlighted here in Table 1.

Computed piezospectroscopic (PS) coefficients are from grain-averaged theories that define the shift as follows (Ma & Clarke, 1993),

$$\overline{\Delta \nu^A} = \frac{1}{3}\left(\Pi_{11} + \Pi_{22} + \Pi_{33}\right)\overline{\Delta \sigma^A}, \qquad (11)$$

where $\overline{\Delta \nu^A}$ is the average shift of the *R*-line peak position, Π_{ii} are the PS coefficients in each crystallographic axis and $\overline{\Delta \sigma^A}$ is the average change in stress.

The PS coefficients reported in Table 1 are measured directly from polycrystalline samples (Ma & Clarke, 1993; Raghavan & Imbrie, 2009) or computed based on (11), where *R*1 and *R*2 are obtained from averaging PS measurements

Table 1
Comparison of our *R*-line PS coefficients (cm^{-1} GPa^{-1}) for the two peaks denoted *R*1 and *R*2 for polycrystalline alumina obtained by calibrating these spectral peaks to stress from X-ray measured strains to those obtained by other researchers through either polycrystalline measurements (*) or computation (+) from single-crystal measurements assuming uniform stress.

Specimen dimensions [Dim; $l \times w \times h$ (mm)] or geometry are provided where available.

	*R*1	*R*2	Dim	Geometry
+ (Schawlow, 1961)	2.6	2.63	–	–
+ (Kaplyanskii & Przhevuskii, 1962)	2.6	2.5	–	Parallelepiped
+ (Feher & Sturge, 1968)	2.4	2.3	–	–
+ (He & Clarke, 1995)	2.53	2.54	$1 \times 1 \times 5$	Parallelepiped
* (Ma & Clarke, 1993)	2.46	2.50	–	Bar
* (Raghavan & Imbrie, 2009)	2.64	2.47	$1.8 \times 2 \times 4$	Parallelepiped

$\frac{1}{3}(\Pi_{11} + \Pi_{22} + \Pi_{33})$ from single-crystal specimens (Schawlow, 1961; Kaplyanskii & Przhevuskii, 1962; Feher & Sturge, 1968; He & Clarke, 1995). In general, the results of these coefficients are in agreement and within the range 2.4–2.64 cm^{-1} GPa^{-1} for the *R*1 peak and 2.3–2.63 cm^{-1} GPa^{-1} for *R*2. However, improvement of resolution for strain measurements using the PS method requires these coefficients to be established with higher accuracy. The inconsistencies in obtaining a uniform stress state in compression testing of high-strength ceramics is a possible explanation of the range of PS coefficients reported and compared here in Table 1. While piezospectroscopic shifts with respect to theoretical stress are reported, often due importance is not given to the dimensions and aspect ratio of the specimens to justify the assumption of uniform compression in these high-strength ceramics. Although the specimens used in some of the experiments are of a parallelepiped configuration, similar to the specimen studied here, the dimensions and aspect ratio may have been different. With a higher aspect ratio, the end effects on the probed location at the center of the specimen may have been alleviated. Along with the aspect ratio, the choice of a cylindrical sample over a parallelepiped specimen for such studies should be assessed and may improve the calibration accuracy for piezospectroscopy.

6. Summary

In general, the uniaxial compressive loading of the alumina specimens which have a high stiffness and are brittle is complicated by effects on the contact surfaces
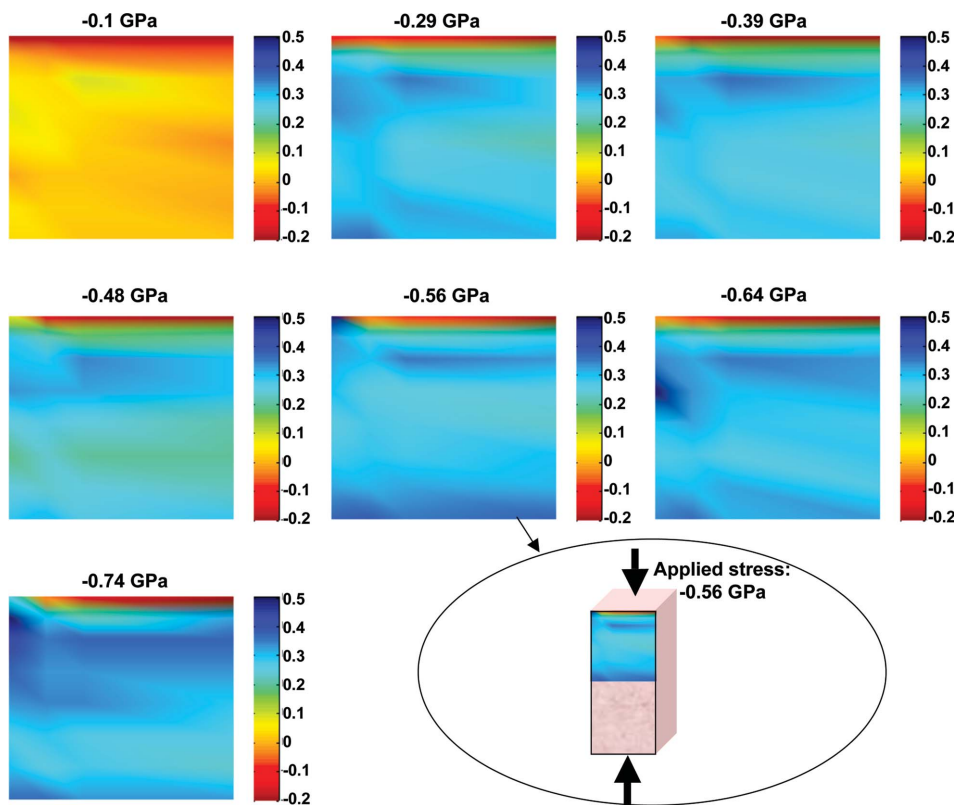

Figure 8
σ_{11} stress map of a half-specimen as viewed from the $\varphi = 90°$ face (obtained from $\varphi = 0°$ data and averaged horizontally across each row to represent the $\varphi = 90°$ direction) at increasing applied compressive stress in the S_3 direction.

during the application of load. The effects of the non-parallelism of the contact surfaces and possibly contact friction were captured using synchrotron X-ray diffraction mapping of the specimen. They were reduced by taking the necessary machining and steps such as lubrication of the surfaces. The sapphire contact platens were used to assist in uniform distribution of the load from the load frame to the specimen. The X-ray stress maps of our polycrystalline material have shown that the end effects have led to a 20% increase in stress in the central location of the polycrystalline alumina specimen. Alternative methods of reducing the contact friction can be evaluated for our specimens such as the use of titanium coating on the ends of the specimen which has been known to reduce friction effects in off-axis compression tests (Bing & Sun, 2005). Further studies using finite element analysis (FEA) have the potential to shed light on the effect of the coefficient of friction at the specimen–platen interface on the stress distribution. FEA also has the potential to predict the effect of the size of specimens on this stress distribution which is useful for studying local stresses on the larger shear specimens. Alternative specimen geometries and adjustment of the aspect ratio are some possible solutions to minimize the end effects on the specimen and improve the calibration of piezospectroscopic coefficients.

References

Abbasova, R., Visintin, S. & Sergo, V. (2005). *J. Mater. Sci.* **40**, 1593–1597.

Almer, J., Lienert, U., Peng, R. L., Schlauer, C. & Oden, M. (2003). *J. Appl. Phys.* **94**, 697–702.

ASTM (1983). *Standard Test Method for Compressive (Crushing) Strength of Fired Whiteware Materials C 773*. Technical Report. Americal Society for Testing and Materials.

ASTM (2002). *Standard Test Method for Compressive Properties of Rigid Plastics D-695 (02a)*. Technical Report. American Society for Testing and Materials.

ASTM (2006). *Standard Test Method for Compressive (Crushing) Strength of Fired Whiteware Materials C 773 - 88* (Reapproved 2006). Technical Report. American Society for Testing and Materials.

Bing, Q. & Sun, C. (2005). *Compos. Sci. Technol.* **65**, 2481–2491.

Buckley, D. H. (1966). *Friction Characteristics of Single Crystal and Polycrystalline Aluminium Oxide in Contact in Vacuum*. Technical Report. NASA.

Castaing, J., Mitchell, T. E. & Rodriguez, A. D. (1998). *Scr. Mater.* **38**, 45–51.

Clarke, D., Christensen, R. & Tolpygo, V. (1997). *Surf. Coat. Technol.* **94–95**, 89–93.

Dolle, H. & Hauk, V. (1977). *Z. Metallkdd.* **68**, 725–728.

Dunlay, W. A., Tracy, C. A. & Perrone, P. J. (1989). *A Proposed Uniaxial Compression Test for High Strength Ceramics*. Technical Report. US Army Materials Technology Laboratory.

Feher, E. & Sturge, M. (1968). *Phys. Rev.* **172**, 244–249.

Forman, R. A., Piermarini, G. J., Barnett, J. D. & Block, S. (1972). *Science*, **176**, 284–285.

Gell, M., Sridharan, S. & Wen, M. (2004). *Int. J. Appl. Ceram. Technol.* **1**, 316–329.

Haeffner, D., Almer, J. & Lienert, U. (2005). *Mater. Sci. Eng A*, **399**, 120–127.

Hammersley, A. P. (1998). ESRF Internal Report. ESRF98HA01T. ESRF, Grenoble, France.

Hauk, V. (1997). *Structural and Residual Stress Analysis by Nondestructive Methods: Evaluation Application, Assessment.* Elsevier Science and Technology Books.

He, J. & Clarke, D. R. (1995). *J. Am. Ceram. Soc.* **78**, 1347–1353.

Jakobsen, B. (2006). PhD thesis, Roskilde University, Denmark.

Jakobsen, B., Poulsen, H. F., Lienert, U. & Pantleon, W. (2007). *Acta Mater.* **55**, 3421.

Kaplyanskii, A. A. & Przhevuskii, A. K. (1962). *Sov. Phys.* **7**, 313–316.

Korsunsky, A., Wells, K. E. & Withers, P. (1998). *Scr. Mater.* **39**, 1705–1712.

Lankford, J. (1977). *J. Mater. Sci.* **12**, 791–796.

Ma, Q. & Clarke, D. R. (1993). *J. Am. Ceram. Soc.* **76**, 1433–1440.

Noyan, I. & Cohen, J. (1987). *Residual Stress*. Berlin: Springer-Verlag.

Nychka, J. A. & Clarke, D. R. (2001). *Surf. Coat. Technol.* **146–147**, 110–116.

Ott, R., Sansoz, F., Molinari, J., Almer, J., Ramesh, K. & Hufnagel, T. (2005). *Acta Mater.* **53**, 1883–1893.

Pagano, N. & Halpin, J. (1968). *J. Compos. Mater.* **2**, 18–31.

Raghavan, S. & Imbrie, P. (2008). *Proceedings of the Material Science and Technology 2008 Conference*, Pittsburgh, PA, USA.

Raghavan, S. & Imbrie, P. K. (2009). *J. Am. Ceram. Soc.* **92**, 1567–1573.

Raghavan, S., Imbrie, P. & Crossley, W. (2008). *Appl. Spectrosc.* **62**, 759–765.

Reiss, R., Yao, T.-M. & Clarke, R. K. (1983). *ASTM STP808: Effect of Load Introduction in Compression Testing of Composite Laminates*. Technical Report. American Society for Testing and Materials.

Schawlow, A. (1961). *Adv. Quantum Electron.* **2**, 50–64.

Tracy, C. A. (1987). *J. Test. Eval.* **15**, 14–19.

Wanner, A. & Dunand, D. (2000). *Metall. Mater. Trans. A*, **31**, 2949–2962.

Zeuch, D. H. (1992). *J. Mater. Res.* **7**, 1956–1959.